Supporting Information

Porosity-Induced Selective Sensing of Iodide in Aqueous Solution by a Fluorescent Imidazolium-Based Ionic Porous Framework

Zixu Chen, Ruixue Sun, Shengyu Feng, Dengxu Wang,* Hongzhi Liu

National Engineering Research Center for Colloidal Materials & Key Laboratory of Special Functional Aggregated Materials, Ministry of Education, School of Chemistry and Chemical Engineering, Shandong University, Jinan, Shandong, 250100, China

*Corresponding author's e-mail: dxwang@sdu.edu.cn

Table of contents

Characterization

intensity of IPF prepared with the reaction time at 12 h (b), 24 h (d), and 36 h (f) suspensions versus the concentration of I^- (1～10 μM).

Figure S9. (a-b) The idealized geometry of IPF sensing Br^- by placing one iodide ion outside (a) and inside the pore (b) optimized by Material studio 8.0 using as the force field.

Figure S10. The pH effect on the detection performance of IPF dispersion in the absence and presence of I^-

Figure S11. Stern–Volmer plot (0～600 μM) for the paper strips in the presence of I^- ($R^2 = 0.9874$)

Figure S12. Plot of emission intensity at 405 nm versus the concentration of I^- (1～10 μM)

Figure S13. BET plot of IPF prepared with the reaction time at 12 h

Figure S14. BET plot of IPF prepared with the reaction time at 24 h

Figure S15. BET plot of IPF prepared with the reaction time at 36 h

Figure S16. BET plot of IPF prepared with the reaction time at 48 h

Table S1. Porosity data of IPF prepared with the reaction times at 12h, 24h, 36h, and 48 h.

Characterization

Fourier transform infrared (FT-IR) spectra was measured within a 4000 to 400 cm^{-1} region on a Bruker TENSOR-27 infrared spectrophotometer (KBr pellet). ^1H NMR and ^{13}C NMR in solution, solid-state ^{13}C cross-polarization/magic-angle-spinning (CP/MAS) NMR and ^{29}Si MAS NMR data were collected on Bruker AVANCE-500 NMR Spectrometer operating at a magnetic field strength of 9.4 T. The resonance

frequencies at this field strength were 125 and 99 MHz for ^{13}C NMR and ^{29}Si NMR, respectively. A chemagnetics 5 mm triple-resonance MAS probe was used to acquire ^{13}C and ^{29}Si NMR spectra. ^{29}Si MAS NMR spectrum with high power proton decoupling was recorded using a $\pi/2$ pulse length of 5 μs, a recycle delay of 120 s and a spinning rate of 5 kHz. Elemental analysis was performed using an Elementar vario EL III elemental analyzer.

Thermogravimetric analysis (TGA) was performed under N_2 using a TA SDTQ600 at a temperature range of room temperature to 800°C with a heating rate of 10°C min^{-1}. Field-emission scanning electron microscopy (FE-SEM) experiments were performed by using HITACHI S4800 Spectrometer. The particle size analysis was performed using a Zetasizer3000 instrument. Powder X-ray diffraction (PXRD) was carried out on a Riguku D/MAX 2550 diffractometer with Cu-Kα radiation, 40 kV, 20 mA with the 2θ range of 10°~80° (scanning rate of 10° min^{-1}) at room temperature. Nitrogen sorption isotherm measurement was performed on a Micro Meritics surface area and pore size analyzer. Before measurement, sample was degassed at 100°C for least 12 h. A sample of ca. 100 mg and a UHP-grade nitrogen (99.999%) gas source were used in the nitrogen sorption measurements at 77 K and collected on a Quantachrome Quadrasorb apparatus. BET surface area was determined over a P/P_0 range from 0.01 to 0.20. Nonlocal density functional theory (NL-DFT) pore size distribution was determined using the carbon/slit-cylindrical pore mode of the Quadrawin software. Ultraviolet absorption (UV) spectrum was determined with TU-1901 double beam UV-vis spectrophotometer. The fluorescence (excitation and emission) spectra of the samples were determined with a Hitachi F-7000 fluorescence spectrophotometer using a monochromated Xe lamp as an excitation source.

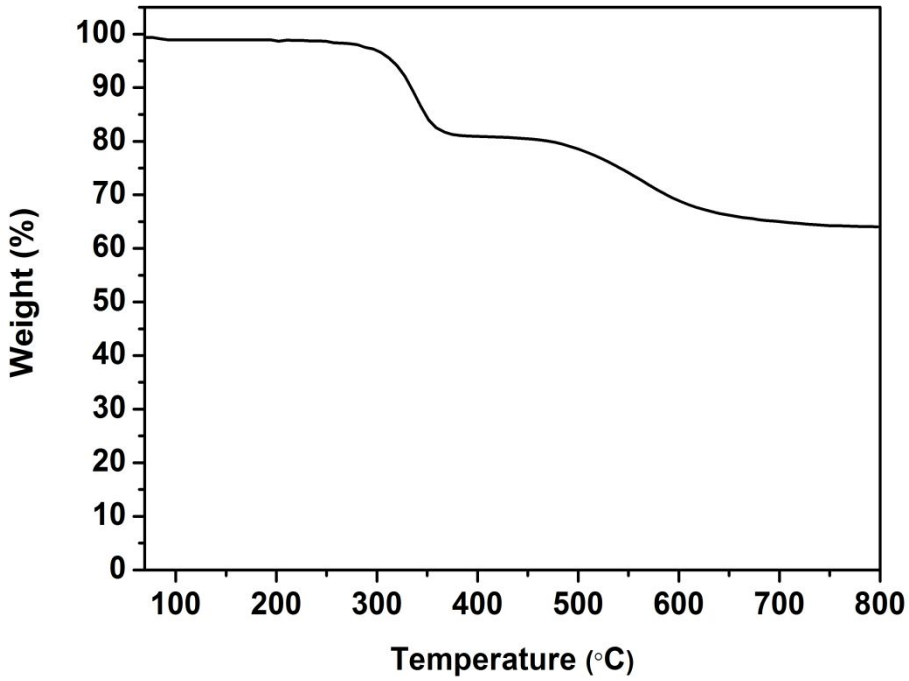

Figure S1. TGA curve of IPF under N_2 atmosphere with a heating rate of 10°C min^{-1}

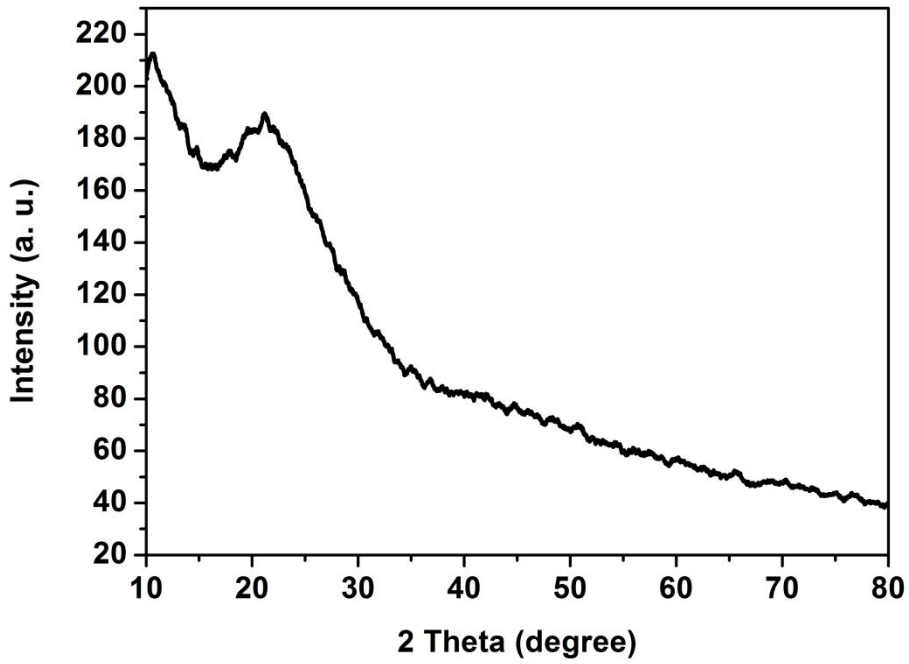

Figure S2. PXRD pattern of IPF

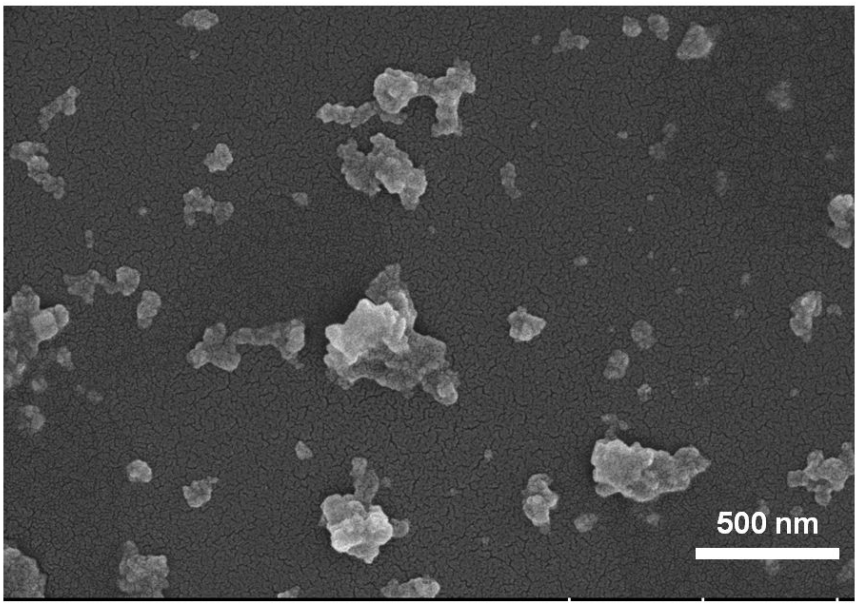

Figure S3. FE-SEM image of IPF

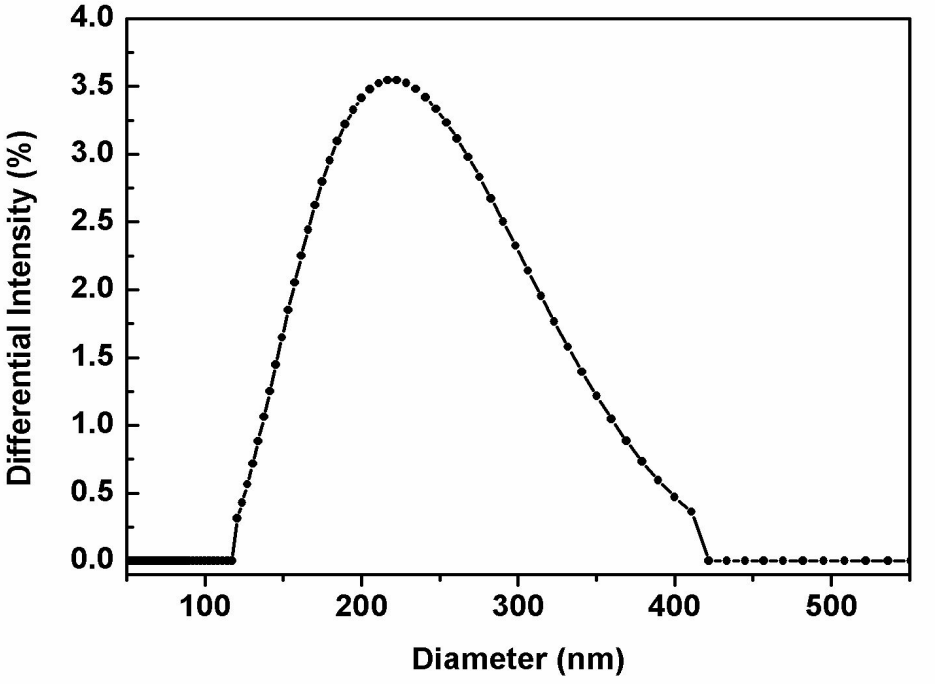

Figure S4. Particle size distribution of IPF suspension in water (5.0 mM)

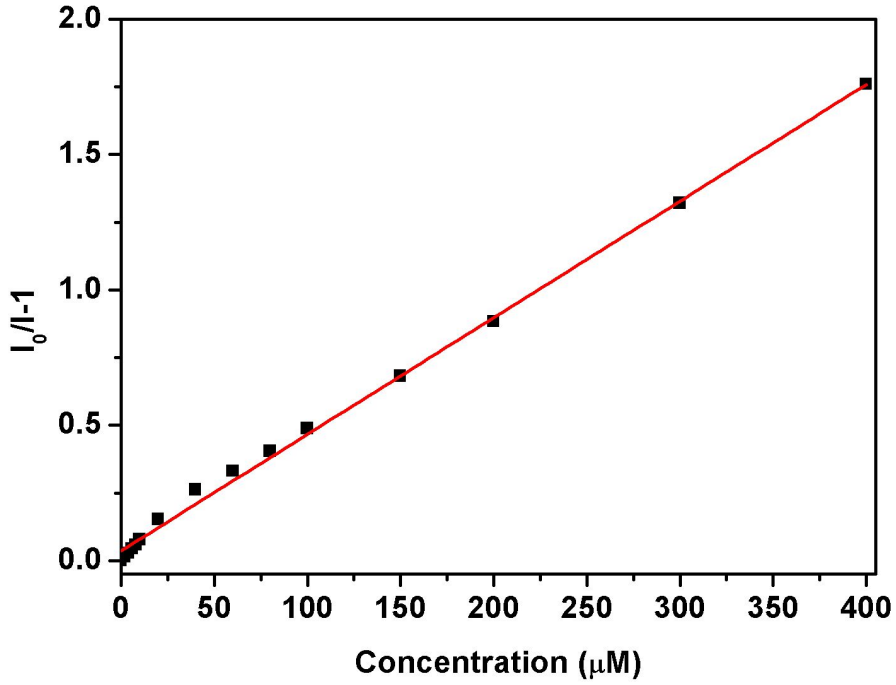

Figure S5. Stern–Volmer plot for IPF dispersion in the presence of I^- ($R^2 = 0.997$)

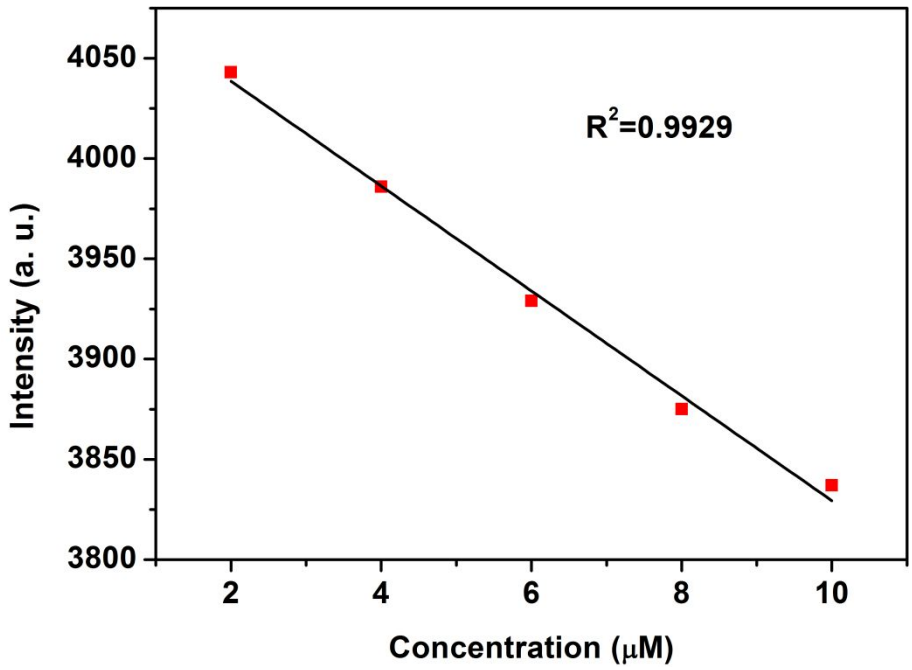

Figure S6. Plot of emission intensity at 400 nm versus the concentration of I^- (1～10 μM)

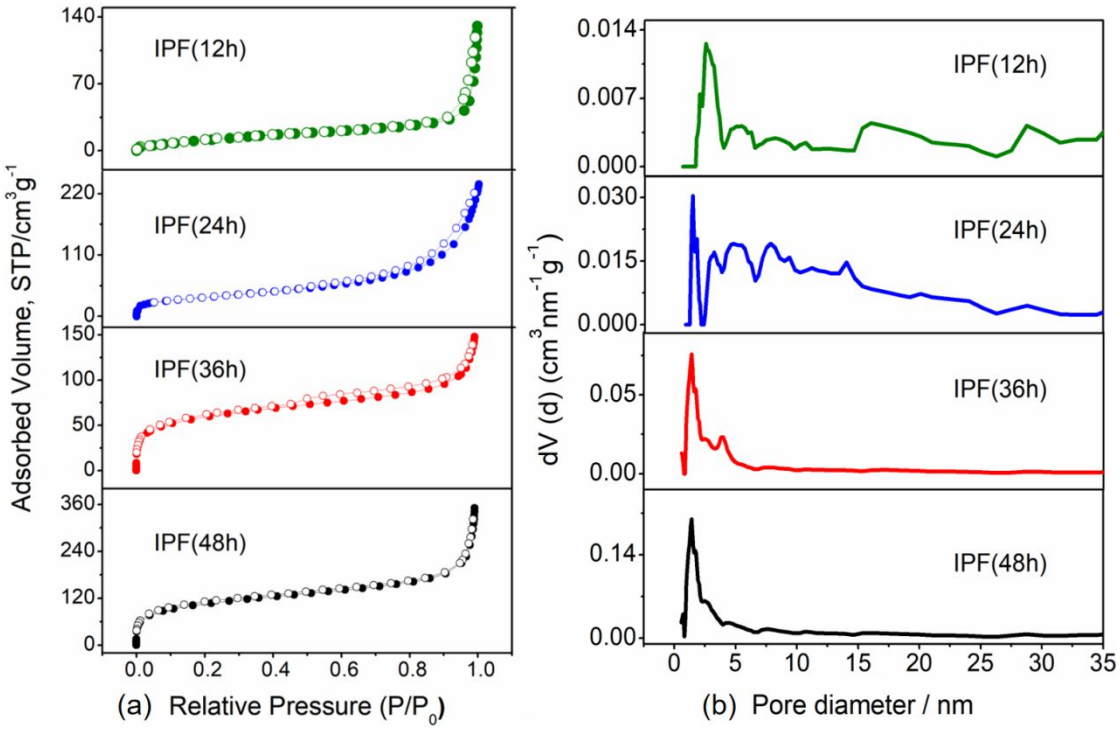

Figure S7. (a-b) Nitrogen adsorption-desorption isotherms (a) and pore size distribution curves (b) of IPF prepared with the reaction times at 12 h, 24 h, 36 h, and 48 h.

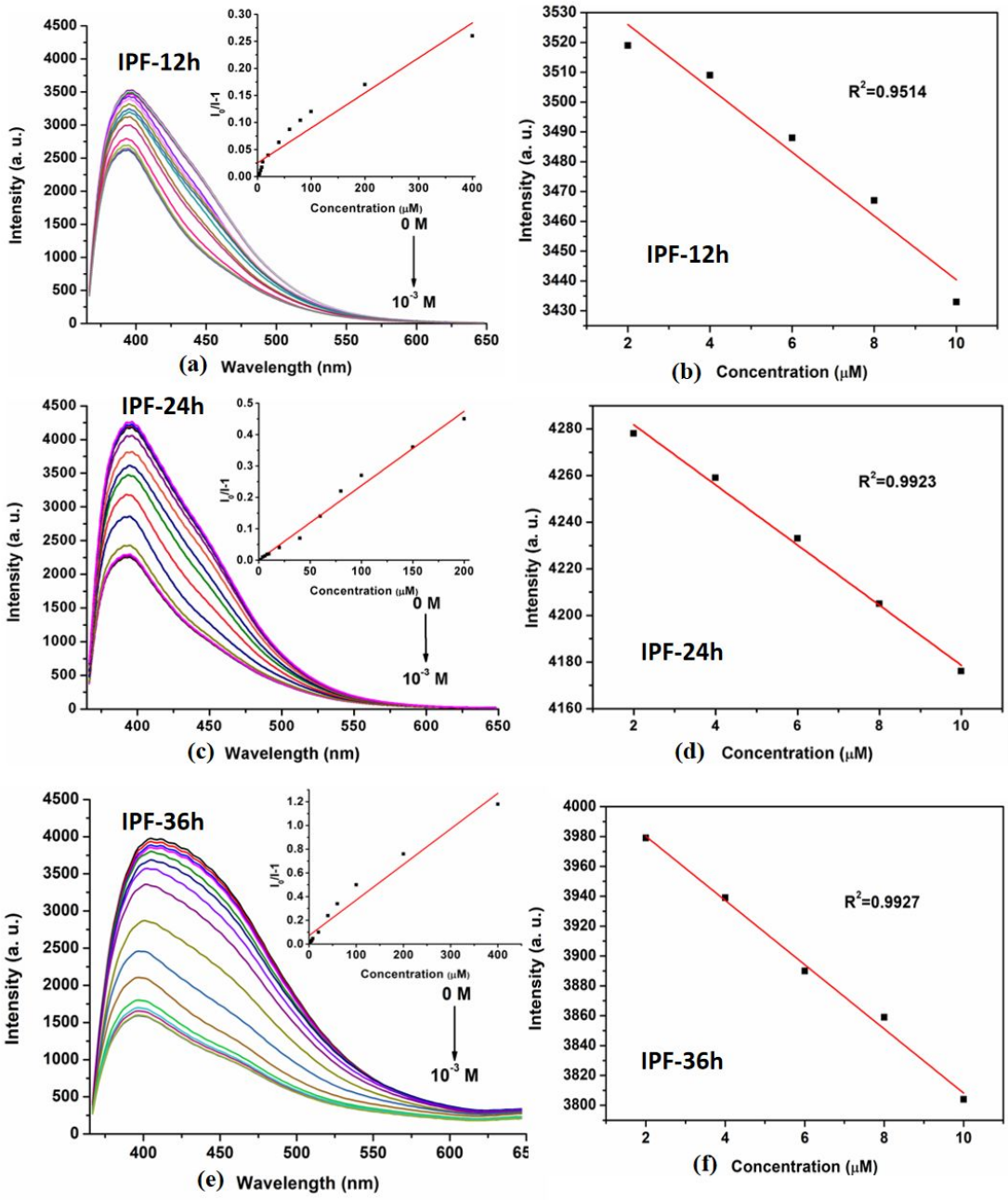

Figure S8. (a, c, e) Fluorescence quenching spectra of IPF prepared with the reaction time at 12 h (a), 24 h (c), and 36 h (e) suspensions in water (0.1 mg/mL) with various concentrations of I^- (0 ~ 1×10^{-3} mol/L, λ_{ex} = 345 nm). The insets show the photographs of Stern–Volmer plot for IPF-12h (R^2 = 0.927), IPF-24h (R^2 = 0.977), IPF-36h (R^2 = 0.952) suspensions in the presence of I^-. (b, d, f) Plot of emission intensity of IPF prepared with the reaction time at 12 h (b), 24 h (d), and 36 h (f) suspensions versus the concentration of I^- (1～10 μM).

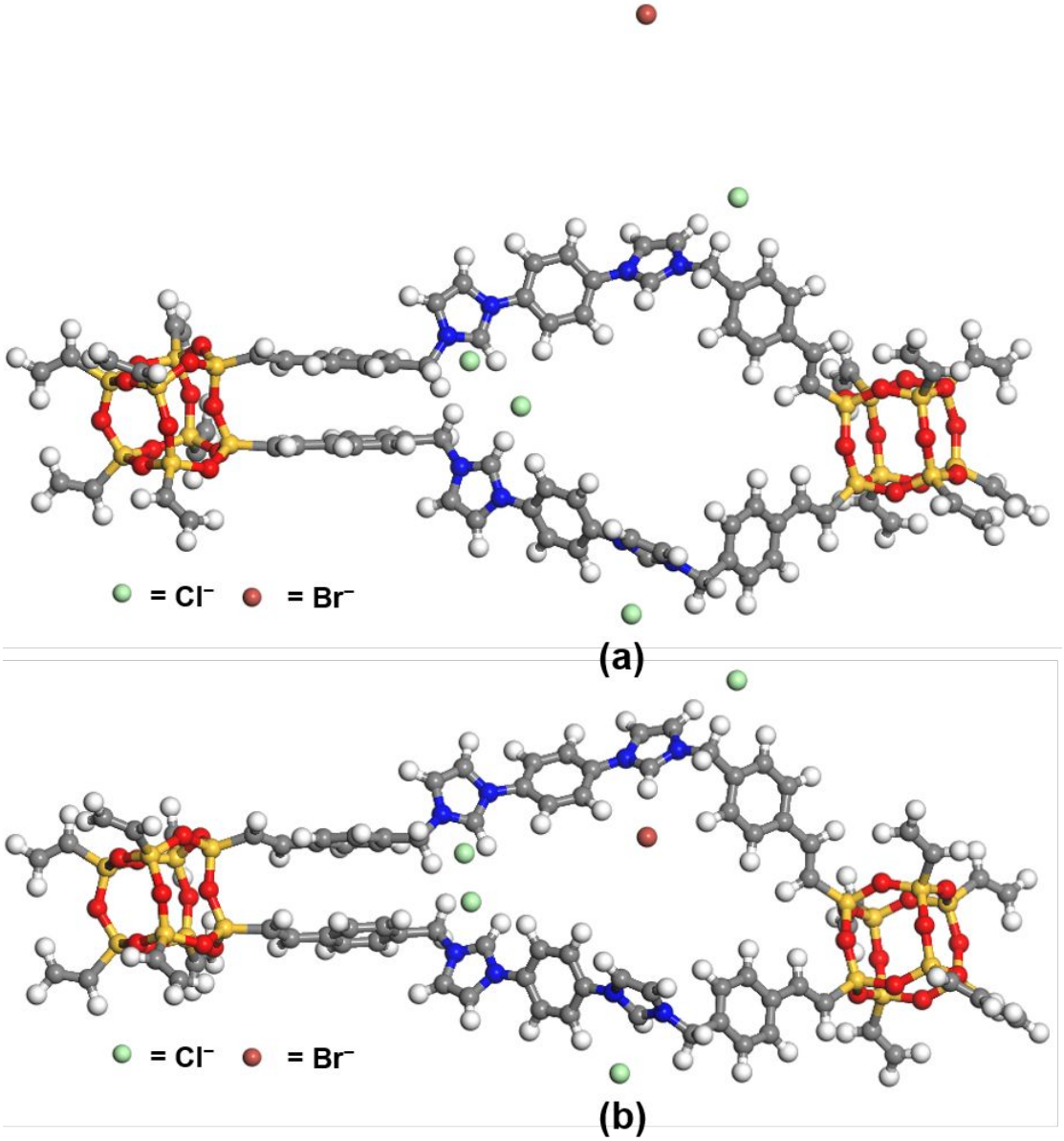

Figure S9. (a-b) The idealized geometry of IPF sensing Br^- by placing one iodide ion outside (a) and inside the pore (b) optimized by Material studio 8.0 using LDA/PWC as the force field (black: carbon atom; white: hydrogen atom; brown: bromine atom; green: chlorine atom; yellow: silicon atom; red: oxygen atom). We hypothesize that no destruction of the cage silsesquioxane units occurred after the formation of porous structure.

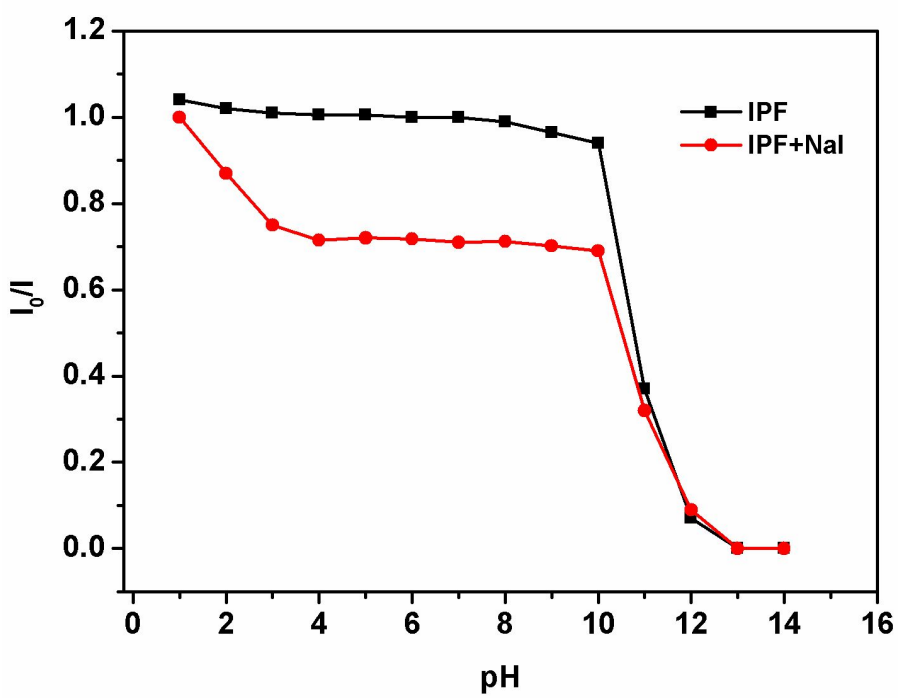

Figure S10. The pH effect on the detection performance of IPF dispersion in the absence and presence of I^-

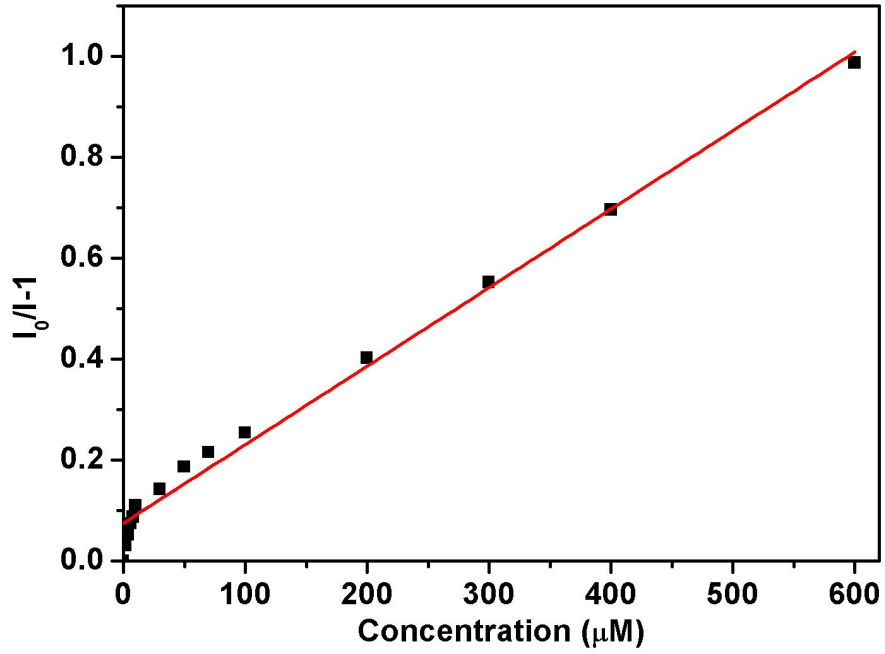

Figure S11. Stern–Volmer plot (0～600 μM) for the paper strips in the presence of I^- ($R^2 = 0.9874$)

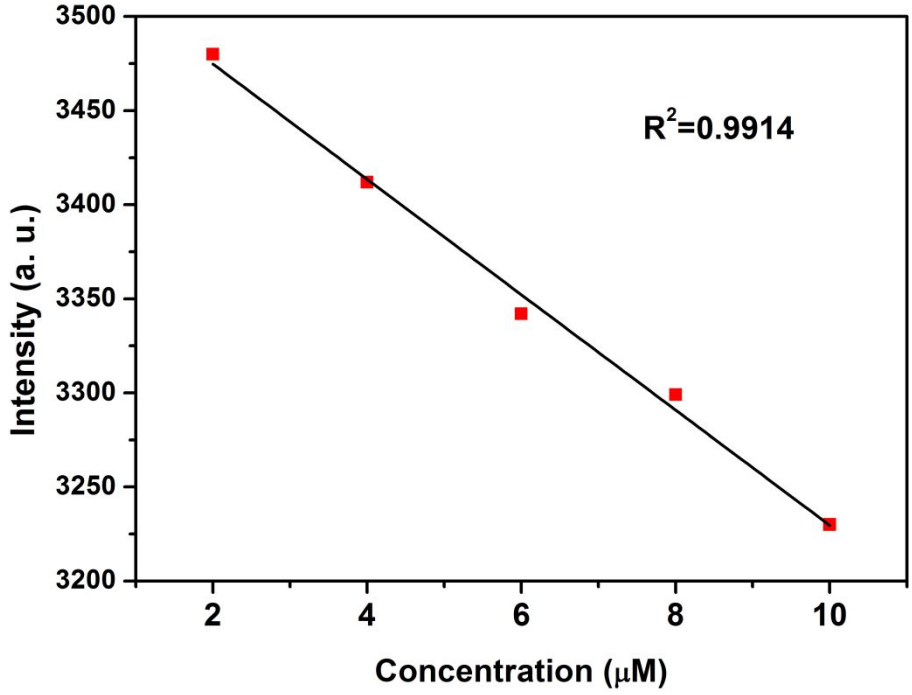

Figure S12. Plot of emission intensity at 405 nm versus the concentration of I^- (1～10 μM)

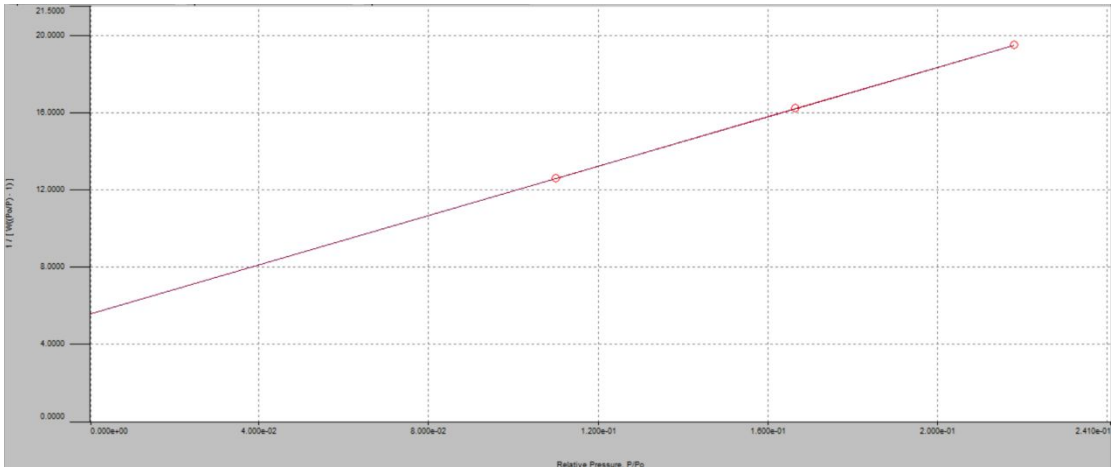

Figure S13. BET plot of IPF prepared with the reaction time at 12 h (r = 0.999998, C = 12.429)

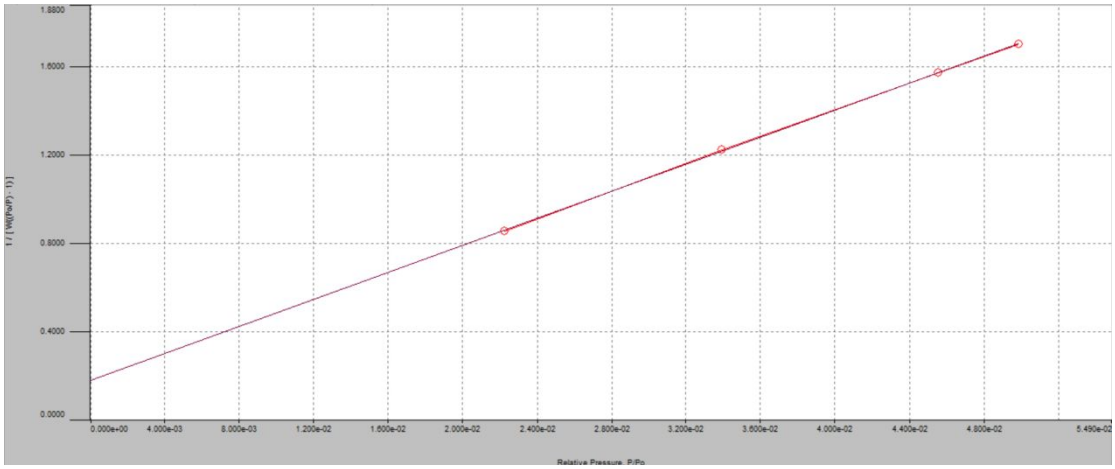

Figure S14. BET plot of IPF prepared with the reaction time at 24 h (r = 0.999908, C = 173.655)

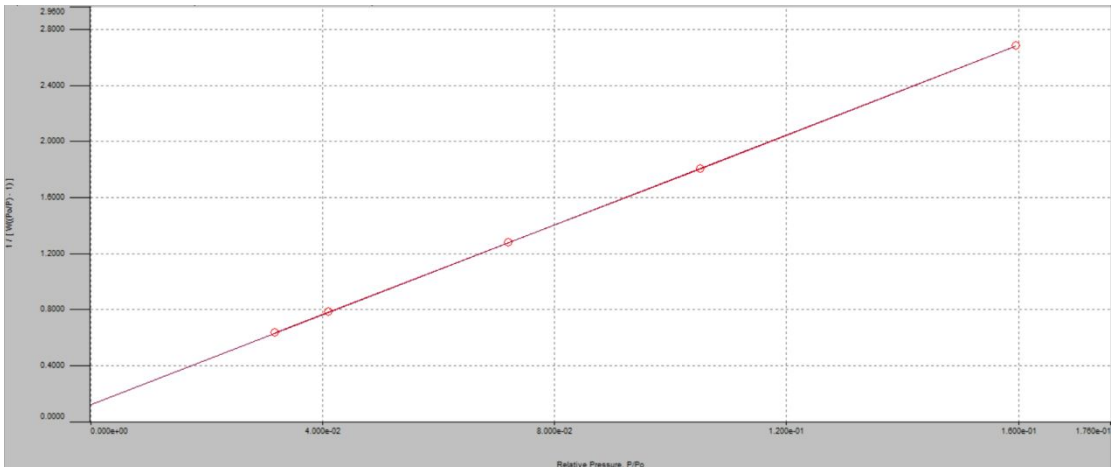

Figure S15. BET plot of IPF prepared with the reaction time at 36 h (r = 0.999988, C = 133.406)

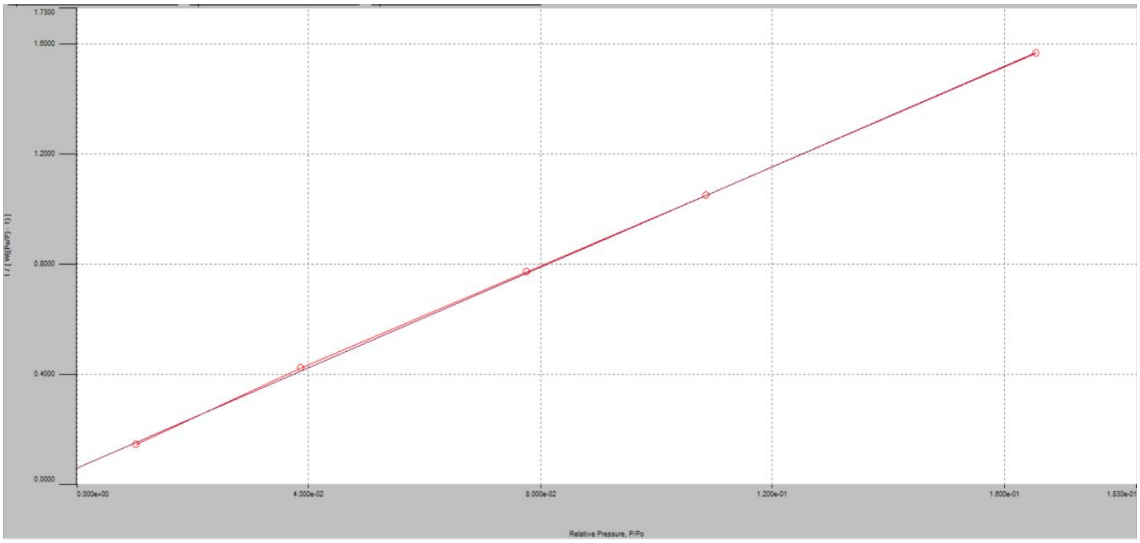

Figure S16. BET plot of IPF prepared with the reaction time at 48 h (r = 0.999901, C = 157.827)

Table S1. Porosity data of IPF prepared with the reaction times at 12 h, 24 h, 36 h, and 48 h.

IPF	S_{BET}[a]/m^2 g^{-1}	S_{micro}[b]/m^2 g^{-1}	V_{total}[c]/cm^3 g^{-1}	V_{micro}[d]/cm^3 g^{-1}	V_{micro}/V_{total}
IPF (12 h)	50	2.95	0.20	0.04	0.2
IPF (24 h)	113	0	0.36	0	0
IPF (36 h)	215	123	0.23	0.05	0.22
IPF (48 h)	379	227	0.53	0.10	0.19

[a] Surface area calculated from N_2 adsorption isotherm using the BET method; [b] Microporous surface area calculated from N_2 adsorption isotherm using *t*-plot method; [c] Total pore volume calculated at P/P_0 = 0.99; [d] Micropore volume derived using the *t*-plot method based on the de Boer thickness equation.